Science Bulletin 70 (2025) 1118–1125

Contents lists available at ScienceDirect

Science Bulletin

journal homepage: www.elsevier.com/locate/scib

Article

A multi-site Ru-Cu/CeO_2 photocatalyst for boosting C-N coupling toward urea synthesis

Qingyu Wang [a,b,1], Yangyang Wan [e,1], Qichen Liu [a,1], Yida Zhang [d], Zhentao Ma [a], Zirui Xu [a], Pengting Sun [e], Gongming Wang [b], Hai-Long Jiang [b], Wenping Sun [c,*], Xusheng Zheng [a,*]

[a] National Synchrotron Radiation Laboratory, University of Science and Technology of China, Hefei 230029, China
[b] College of Chemistry and Materials Science, University of Science and Technology of China, Hefei 230026, China
[c] School of Materials Science and Engineering, Zhejiang University, Hangzhou 310058, China
[d] College of Chemical Engineering, Inner Mongolia University of Technology, Hohhot 010051, China
[e] School of Materials Science and Engineering, Jiangsu University, Zhenjiang 212013, China

ARTICLE INFO

Article history:
Received 29 October 2024
Received in revised form 22 December 2024
Accepted 17 January 2025
Available online 31 January 2025

Keywords:
Multi-site photocatalyst
Photocatalytic urea synthesis
C-N coupling
Carrier separation
Molecular activation

ABSTRACT

Photocatalytic urea production from nitrogen (N_2) and carbon dioxide (CO_2) is a sustainable and eco-friendly alternative to the Bosch-Meiser route. However, it remains a significant challenge in developing highly efficient photocatalysts for enhancing C-N coupling to high-yield urea synthesis. Herein, we propose a multi-site photocatalyst concept to address the concern of low yield by simultaneously improving photogenerated carrier separation and reactant activation. As a proof of concept, a well-defined multi-site photocatalyst, Ru nanoparticles and Cu single atoms decorated CeO_2 nanorods (Ru-Cu/CeO_2), is developed for efficient urea production. The incorporation of Ru and Cu sites is crucial not only to generate high-density photogenerated electrons, but also to facilitate N_2 and CO_2 adsorption and conversion. The *in situ* formed local nitrogen-rich area at Ru sites increases the encounter possibility with the carbon-containing species generated from Cu sites, substantially promoting C-N coupling. The Ru-Cu/CeO_2 photocatalyst exhibits an impressive urea yield rate of 16.7 μmol g^{-1} h^{-1}, which ranks among the best performance reported to date. This work emphasizes the importance of multi-site catalyst design concept in guaranteeing rapid C-N coupling in photocatalytic urea synthesis and beyond.

© 2025 Science China Press. Published by Elsevier B.V. and Science China Press. All rights are reserved, including those for text and data mining, AI training, and similar technologies.

1. Introduction

As an indispensable nitrogen fertilizer, urea has greatly underpinned the agricultural production and the expanding populations [1–7]. Industrial urea production primarily relies on the Bosch-Meiser protocol with ammonia (NH_3) and carbon dioxide (CO_2) as feed gases [8–12]. The harsh conditions of high temperature (>150 °C) and pressure (>15 MPa) cause tremendous energy consumption and industrial pollutants [13–16]. By contrast, converting nitrogen (N_2) and CO_2 into urea under mild conditions through photocatalytic C-N coupling has emerged as an alternative route for urea production [17–20]. Unfortunately, this sustainable and eco-friendly urea synthetic approach still suffers from low yield. Thus, it is urgently desired to develop efficient photocatalysts for promoting C-N coupling between N_2 and CO_2 to produce urea at high yield, which remains a great challenge.

In virtue of the chemical inertness of N_2 and CO_2 molecules, the way to boost molecular activation has triggered extensive contemplation, especially through the structural design of photocatalysts. For instance, heterostructure and defect engineering have been employed to functionalize photocatalysts, facilitating molecular activation or stabilizing the key intermediate of *NCON in urea synthesis [18,19]. On the other hand, efforts have also been made to enrich photogenerated electrons to improve the conversion efficiency, which is also a common strategy in the photocatalysis field [21]. However, current works still focus on the single-solution approaches, together with the unsatisfactory C-N coupling efficiency from the random molecular collisions, which leads to limited catalytic activity in urea photosynthesis. Therefore, it would provide more potential to accelerate urea production if constructing a multi-site photocatalyst of boosting the activation and coupling of N_2 and CO_2, along with enhancing the separation of photogenerated carriers.

* Corresponding authors.
E-mail addresses: wenpingsun@zju.edu.cn (W. Sun), zxs@ustc.edu.cn (X. Zheng).
[1] These authors contributed equally to this work.

https://doi.org/10.1016/j.scib.2025.01.059
2095-9273/© 2025 Science China Press. Published by Elsevier B.V. and Science China Press. All rights are reserved, including those for text and data mining, AI training, and similar technologies.

Herein, we develop a multi-site photocatalyst, consisting of CeO_2 nanorods decorated with Ru nanoparticles and Cu single atoms (Ru-Cu/CeO_2), for the purpose of synthesizing urea at high yield. Notably, Ru and Cu sites promote photogenerated carrier separation and migration in CeO_2, which benefits the ample electron supply for the co-reduction process of N_2 and CO_2 into urea. Meanwhile, Ru and Cu sites exhibit specific affinity for N_2 and CO_2, respectively, enabling efficient site-selective molecular activation. The nitrogen-rich Ru site realizes the spontaneous coupling with CO intermediate, significantly elevating urea synthesis efficiency (Scheme 1). This work highlights the potential of multi-site catalyst design for simultaneously optimizing molecular and electron behavior in photocatalytic ure production and other catalysis.

2. Materials and methods

2.1. Instrumentations

X-ray diffraction (XRD) patterns were recorded over a TTR-III X-ray diffractometer with Cu-Kα radiation to obtain the crystal structure of samples. Inductively coupled plasma atomic emission spectroscopy (ICP-AES, iCAP 7400) was carried out for the element content analysis of samples. Transmission electron microscopy (TEM, JEM-2100F) and magnified high-angle-annular-dark-field scanning transmission electron microscopy (HAADF-STEM, JEM-ARM200F) were employed to explore the micromorphology of the catalysts. High-resolution mass spectroscopy (HRMS) tests were carried out over LTQ Orbitrap XL mass spectrometer. Nuclear magnetic resonance (NMR) spectra were collected by a Bruker AVANCE AV III 400 spectrometer. Photoelectrochemical measurement was carried out on an electrochemical station (CHI 660E) with Pt foil and Ag/AgCl as the counter and reference electrode, respectively. Transient absorption spectroscopy (TAS) measurements were conducted based on a motorized optical delay line-equipped transient absorption spectrometer (Helios, Ultrafast system). X-ray photoelectron spectroscopy (XPS) and *in situ* diffuse reflectance infrared Fourier transform spectroscopy (DRIFTS) experiments were performed at BL10B and BL01B beamlines of Hefei Light Source (HLS) in Hefei, China, respectively.

2.2. Chemicals

Cerium chloride ($CeCl_3$), ruthenium chloride ($RuCl_3$), copper chloride ($CuCl_2$), sodium borohydride ($NaBH_4$), sodium hydroxide (NaOH), and ethanol (EtOH) were purchased from Aladdin Biochemical Technology Co., Ltd. CO_2 (≥99.999%) and N_2 (≥99.999%) were purchased from Nanjing Shangyuan Industrial Gas Co. Ltd. $^{13}CO_2$ (≥98%) and $^{15}N_2$ (≥98%) isotopes were produced by Wuhan Newradar Special Gas Co. Ltd.

2.3. Preparation of CeO_2

The 0.76 g of $CeCl_3{\cdot}7H_2O$ (solution A) and 8.44 g of NaOH (solution B) were respectively dispersed into 20 and 15 mL of deionized water, respectively. Solution B was added to solution A by a peristaltic pump with the flow velocity of 30 mL h^{-1} under stirring and reacted for 30 min, followed by being kept at 100 °C overnight. The mixture was cooled down and washed with ethanol and deionized water, then freeze-dried and annealed in Ar at 500 °C for 4 h to obtain CeO_2.

2.4. Preparation of Ru-Cu/CeO_2, Ru/CeO_2, and Cu/CeO_2

As for Ru-Cu/CeO_2, 30-mg CeO_2 was added into 20-mL deionized water, and then sonicated for 0.5 h. 18.7 μL of $RuCl_3$ solution (0.19 mmol L^{-1}) and 61.4 μL of $CuCl_2$ solution (0.05 mmol L^{-1}) were added under stirring, then added 10 mL of $NaBH_4$ solution (0.26 mol L^{-1}) with the flow velocity of 20 mL h^{-1}. The product after 2-h reaction was collected by centrifugation. As for Ru/CeO_2 and Cu/CeO_2, only the corresponding precursor solution was added into the suspension during the synthesis process.

2.5. Catalytic tests

The photocatalytic urea synthesis was conducted in a 15-mL self-made photocatalytic reactor. 10-mg photocatalysts were dispersed in 3-mL deionized water, followed by bubbling with the mixed gas (CO_2/N_2 = 1:1) for 30 min. The feeding gas was already purified successively through H_2SO_4, $KMnO_4$, and KOH solution to remove the potential NO_x and NH_3. Then the reactor was pumped to vacuum, followed by injecting 60 mL of mixed gas into the reactor. The suspension was illuminated by a Xenon lamp under continuous stirring. The yields of the liquid products were calculated from the chromogenic methods, NMR, and high performance liquid chromatography (HPLC) tests, respectively. The gaseous product was detected by gas chromatography.

2.6. X-ray absorption fine spectroscopy (XAFS)

XAFS tests at Ru K-edge (E_0 = 22117 eV) and Cu K-edge (E_0 = 8979 eV) were performed at beamline BL14W1 of Shanghai Synchrotron Radiation Facility. Athena and Artemis codes were applied for data simulation. During the *in situ* XAFS tests, the tested sample was immersed into H_2O solution containing N_2 and CO_2 with light irradiation.

2.7. Temperature programmed desorption (TPD) tests

TPD tests were carried out on a VDsorb-91i chemisorption analyzer. During N_2-TPD measurement, 50 mg of the sample was pretreated by the He gas flow for 1 h at 350 °C, followed by cooling to room temperature. N_2 adsorption was then carried out with N_2 gas flow at 350 °C for 1.5 h. Afterwards, the sample was purged with He for 0.5 h to remove the residual N_2, along with the temperature being increased from 50 to 750 °C at a rate of 10 °C min^{-1}. CO_2-TPD tests were similar to N_2-TPD, except for the adsorbate. The desorption profiles of adsorbed gas were recorded by a thermal conductivity detector (TCD).

2.8. Density functional theory (DFT) calculations

Our computational approach relied on DFT calculations with the Vienna Ab Initio Package [22–24], employing the Perdew-Burke-Ernzerhof functional within the generalized gradient approximation [25,26]. Plane wave descriptions were terminated at a500-eV cutoff energy, and Brillouin zone sampling utilized specific *k*-point meshes: 3 × 3 × 1 and 4 × 4 × 1 for Ru and CeO_2 surface, respectively. During the optimization, the bottom two layers of Ru atoms were fixed at the bulk lattice positions. As for CeO_2 model, the bottom four layers were fixed. To prevent periodic interactions in slab calculations, we included a vacuum layer with a thickness exceeding 15 Å. Optimization of surface and adsorbed species was conducted with the energy set below 10^{-5} eV and the force convergence criteria below 0.02 eV $Å^{-1}$, respectively. van der Waals interactions were incorporated by DFT-D3 method and BJ-Damping [27]. For the free energy variations calculation, we conducted a computational hydrogen electrode model according to the expression by VASPKIT with the consideration of spin polarization: $\Delta G = \Delta E + \Delta ZPE - T\Delta S + \Delta U(0 \rightarrow T)$, where ΔE denotes adsorption energy, ΔZPE represents zero-point energy, ΔS corresponds to entropy change at a temperature of 298 K, and ΔU

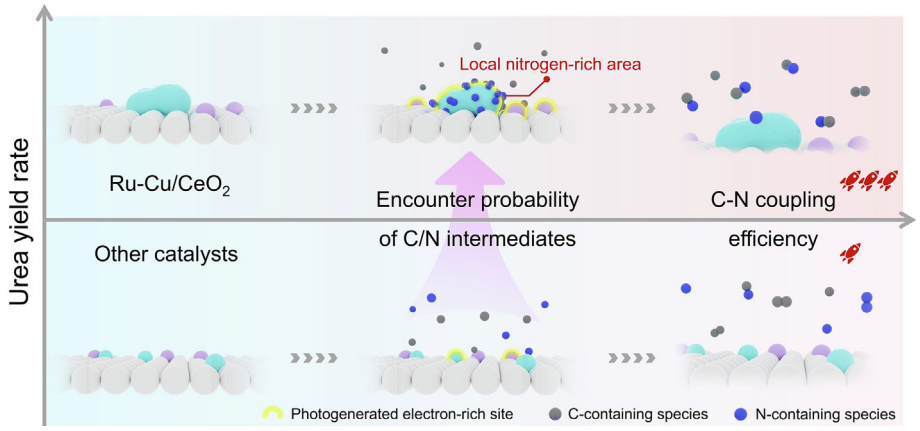

Scheme 1. The comparison between the designed Ru-Cu/CeO_2 catalysts (above) and the reported multi-site catalysts (below) during urea synthesis.

(0→*T*) means the thermal correction to the internal energy [28,29]. Zero-point energy and entropy for adsorbents were determined by vibrational frequency calculations using density functional perturbation theory [30], while entropy values for gaseous species were sourced from the Computational Chemistry Comparison and Benchmark Database.

3. Results and discussion

CeO_2 nanorods were prepared via the hydrothermal method (Figs. S1 and S2 online). Ru and Cu species were further deposited on CeO_2 to obtain Ru-Cu/CeO_2 via a wet chemical process. For comparison, CeO_2 decorated individually decorated with Ru (Ru/CeO_2) and Cu (Cu/CeO_2) were also prepared. ICP-AES results imply that the mass contents of Ru in Ru/CeO_2 and Ru-Cu/CeO_2 were 0.49wt % and 0.51wt%, respectively. The mass contents of Cu in Cu/CeO_2 and Ru-Cu/CeO_2 were calculated as 0.24 wt% and 0.20 wt%, respectively. XRD patterns of the obtained samples are well indexed to the fluorite structure of CeO_2 (Fig. S3 online). We further performed the TEM images of the samples. Cu/CeO_2 retained the nanorod morphology with no obvious nanoparticles (Fig. S4 online). As for Ru/CeO_2 and Ru-Cu/CeO_2, Ru nanoparticles were uniformly dispersed over CeO_2 (Figs. S5 and S6 online). The average size of nanoparticles was determined as approximately 4 nm (Fig. 1a and Fig. S7 online). In addition, we applied the HAADF-STEM characterization for Ru-Cu/CeO_2. As depicted in Fig. 1b, the lattice spacings of 2.7 and 3.1 Å correspond to the (001) facet of Ru nanoparticle and (111) facet of CeO_2, respectively [31,32]. Considering that the lower atomic mass of Cu atoms to those of Ru and Ce leads to difficulties in distinguishing the form of Cu species in Ru-Cu/CeO_2, energy dispersive X-ray spectroscopy (EDS) elemental mapping was further collected (Fig. 1c). Evidently, Ru element displays localized agglomeration at nanoparticle sites, while Cu one is homogeneously distributed over CeO_2 substrate.

Furthermore, we conducted electronic measurements of the obtained samples. As for Ru 3p XPS spectra, the doublet located at 462.3 and 484.5 eV belongs to Ru^0 species (Fig. S8 online) [33]. The peaks with the binding energies of 463.7 and 486.2 eV were attributed to Ru^{4+}, resulting from the unavoidable surficial oxidation of Ru nanoparticles [33,34]. Fig. S9 (online) illustrates Cu 2p XPS spectra for Cu/CeO_2 and Ru-Cu/CeO_2, where the peaks at 954.7 and 934.7 eV correspond to the $2p_{1/2}$ and $2p_{3/2}$ peak of Cu^{2+} species, respectively [35]. Furthermore, XAFS was conducted to reveal the precise structural information of the samples. Ru K-edge X-ray absorption near-edge structure (XANES) spectra of Ru/CeO_2 and Ru-Cu/CeO_2 display the absorption edge positions close to that of Ru foil, manifesting the slight oxidation of Ru species, which are accordant with Ru 3p XPS results (Fig. S10 online). The oxidation states of Cu species in Cu/CeO_2 and Ru-Cu/CeO_2 were estimated as +2 from Cu K-edge XANES profiles (Fig. S11 online). The local coordination environment of Ru and Cu species was further identified by the Fourier-transformed extended X-ray absorption fine structure (FT-EXAFS) analyses (Figs. S12 and S13 online). For Ru/CeO_2 and Ru-Cu/CeO_2, the peaks at 1.5 and 2.4 Å in *R* space correspond to the Ru-O and Ru-Ru shells, respectively (Fig. 1d and Fig. S14 online). The Ru-O coordination originates from the surficial oxidation of Ru nanoparticles [34]. The fitting results further validated the coexistence of Ru-O and Ru-Ru coordination in Ru-Cu/CeO_2 (Table S1 online). The *R*-space curves of Cu/CeO_2 and Ru-Cu/CeO_2 display a prominent peak at 1.5 Å, which is attributed to the Cu-O coordination (Fig. 1e and Table S2 online). The absence of Cu-Cu coordination indicates that the Cu species exist as isolated single atoms. The above results confirm that Ru-Cu/CeO_2 is composed of Ru nanoparticles and Cu single atoms (Fig. 1f).

The photocatalytic performance of the obtained samples in urea synthesis was evaluated (Figs. S15–S21 online). As depicted in Fig. 2a, CeO_2 exhibited a urea yield rate of 3.6 μmol g^{-1} h^{-1}. Upon loading Ru nanoparticles or Cu single atoms, the activity increased with varying extents. The urea yield rates over Ru/CeO_2 and Cu/CeO_2 enhanced to 7.0 and 5.3 μmol g^{-1} h^{-1}, respectively. The combination of Ru nanoparticles and Cu single atoms contributed to the optimal urea yield rate of 16.7 μmol g^{-1} h^{-1}, ranking among the best activity reported in photocatalytic urea synthesis (Table S3 online). The almost consistent urea yield rate calculated from different tests indicates that the generated urea does not result from the errors of measurement method (Table S4 online). The main by-products were detected as NH_3 (0.3 μmol g^{-1} h^{-1}) and CO (8.9 μmol g^{-1} h^{-1}). Consequently, the urea selectivity over Ru-Cu/CeO_2 is determined as 84.3% (Table S5 online). To further assure the authenticity of urea production, a succession of control tests was performed. As shown in Fig. S22 (online), urea was undetectable without Ru-Cu/CeO_2, without light, or by replacing feeding gas with Ar. Additionally, the negligible urea yield with NH_3 and CO_2 as reactants excludes the possibility of the NH_3-mediated urea synthesis pathway. We further conducted the isotopic labeling tests via using $^{15}N_2$ or/and $^{13}CO_2$ as the feeding gas. The products were analysed by HRMS. As shown in Fig. 2b, the signals with mass-to-charge ratios of 61.04, 62.04, 63.03, and 64.01 are assigned to $^{12}CO(^{14}NH_2)_2$, $^{13}CO(^{14}NH_2)_2$, $^{12}CO(^{15}NH_2)_2$, and $^{13}CO(^{15}NH_2)_2$ products, respectively. The results match well with the reactant conditions of $^{12}CO_2$ and $^{14}N_2$, $^{13}CO_2$ and $^{14}N_2$, $^{12}CO_2$ and $^{15}N_2$, $^{13}CO_2$ and $^{15}N_2$, respectively, confirming that urea was synthesized from CO_2 and N_2. This point is further corroborated by

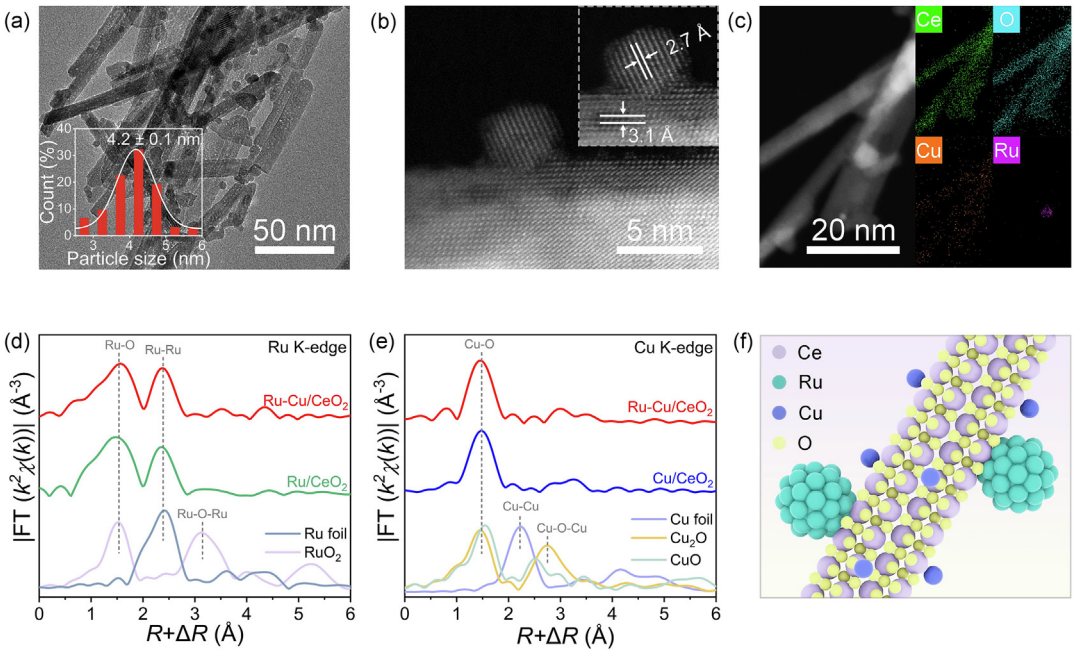

Fig. 1. Multi-site structure analyses of Ru-Cu/CeO_2. (a) TEM image of Ru-Cu/CeO_2. Inset: the statistical analysis of the particle size in (a). (b) HAADF-STEM image of Ru-Cu/CeO_2. (c) EDX elemental mapping images of Ru-Cu/CeO_2. (d) Ru K-edge FT-EXAFS spectra of Ru/CeO_2 and Ru-Cu/CeO_2 in *R* space. (e) Cu K-edge FT-EXAFS spectra of Cu/CeO_2 and Ru-Cu/CeO_2 in *R* space. (f) Structural schematic diagram of Ru-Cu/CeO_2.

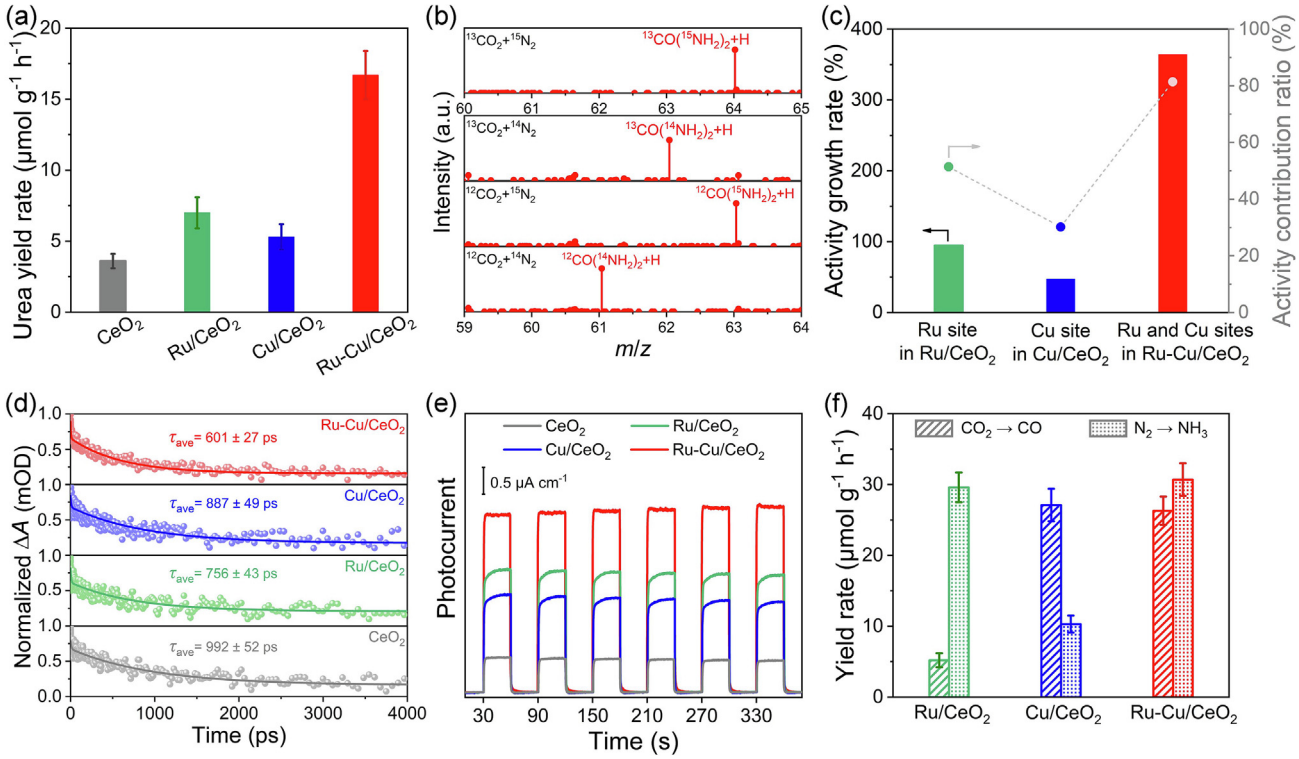

Fig. 2. Catalytic performance and the roles of the multiple sites in Ru-Cu/CeO_2. (a) The yield rates of urea over CeO_2, Ru/CeO_2, Cu/CeO_2, and Ru-Cu/CeO_2. (b) The HRMS spectra for urea production over Ru-Cu/CeO_2 with $^{12}CO_2$ and $^{14}N_2$, $^{13}CO_2$ and $^{14}N_2$, $^{12}CO_2$ and $^{15}N_2$, $^{13}CO_2$ and $^{15}N_2$ as feeding gases, respectively. (c) The activity growth rate compared with CeO_2 (left axis) and the activity contribution ratio (right axis) over Ru site in Ru/CeO_2, Cu site in Cu/CeO_2, and Ru and Cu sites in Ru-Cu/CeO_2. (d) TAS spectra of CeO_2, Ru/CeO_2, Cu/CeO_2, and Ru-Cu/CeO_2. (e) Transient photocurrent responses spectra of the obtained catalysts under Ar atmosphere. (f) The yield rate of CO and NH_3 over Ru/CeO_2, Cu/CeO_2, and Ru-Cu/CeO_2 with CO_2 or N_2 as feeding gas.

the ^{1}H and ^{13}C NMR spectroscopy results (Fig. S23 online). In addition, no evident degradation in urea yield rate was observed after six successive cycles, as well as that the structure was well maintained, validating the stability of Ru-Cu/CeO_2 (Figs. S24 and S25 online).

The origin of the remarkable activity of Ru-Cu/CeO_2 was disclosed by decoupling the role of different reaction sites. As shown in Fig. S26 (online), the electronic structure of CeO_2 was slightly impacted by the introduction of Cu single atoms but almost remained after loading Ru nanoparticles. To distinguish whether the activity improvement originated from the change from CeO_2, we added 10 mmol L^{-1} of KSCN into the reaction solution for inactivating metal active centers. As depicted in Fig. S27 (online), the urea yield rates over Ru/CeO_2, Cu/CeO_2, and Ru-Cu/CeO_2 after the poisoning treatment to Ru and Cu sites were comparable to that over CeO_2. Thus, we attribute the catalytic activity improvement to the decoration of Ru and Cu sites. Among them, the activity contribution from the incorporation of Ru and Cu sites accounted for up to 81.4% in Ru-Cu/CeO_2, significantly exceeding the ones of single Ru or Cu sites (Fig. 2c). Meanwhile, the addition of Ru nanoparticles and Cu single atoms elevated the activity of CeO_2 by 94.4% and 47.2%, respectively. Notably, the catalytic activity was enhanced by over 360% after co-loading Ru and Cu sites. This remarkable augmentation confirms that the synergistic effect between Ru and Cu sites plays a key role in improving urea synthesis performance.

Then, we explored the specific promoting effect of Ru and Cu sites during the photocatalytic urea synthesis. The optical properties of the catalysts were analysed by diffuse reflectance ultraviolet-visible (UV-vis) spectra. As shown in Fig. S28 (online), CeO_2 exhibits a similar photo-response curve as the previous report [18]. The loading of Ru nanoparticles and Cu single atoms both improved the light-absorbing capability and optimized the bandgap of CeO_2 (Figs. S29 and S30 online). Meanwhile, TAS was utilized to investigate the electron dynamics after the introduction of Ru and Cu sites. During the TAS test, the pump pulses with the central wavelength of 340 nm were applied to guarantee the effective excitation of photogenerated photoelectrons. We averaged similar temporal profiles in the range of 420–440 nm and fitted the transient absorption trace (Fig. 2d and Table S6 online). The average decay time (τ_{ave}) for CeO_2 was fitted as (992 ± 52) ps. After the decoration of Ru or Cu sites, their values of τ_{ave} both showed a slight decrease to (756 ± 43) ps and (887 ± 49) ps in Ru/CeO_2 and Cu/CeO_2, respectively. It is noteworthy that Ru-Cu/CeO_2 achieved the shortest τ_{ave} of (601 ± 27) ps with a roughly 40% decrease compared with that of CeO_2. Generally, the shortened τ_{ave} corresponds to the accelerated electron transfer kinetics [36,37]. Obviously, the decoration of Ru or Cu sites constructed an additional electron-transfer channel, elevating the carrier migration efficiency. And the co-loading of Ru and Cu species helped realize the optimal electron dynamics in Ru-Cu/CeO_2. This point is supported by electrochemical impedance spectroscopy (EIS) results (Fig. S31 online) [38]. As for the steady-state photoluminescence (PL) tests, Ru/CeO_2, Cu/CeO_2, and Ru-Cu/CeO_2 exhibited apparently weakened signal intensities compared to that of CeO_2, implying that the Ru and Cu incorporation substantially inhibits the carrier recombination (Fig. S32 online) [37]. Among them, the lowest intensity of Ru-Cu/CeO_2 indicates the most effective carrier separation, which is consistent with the highest photocurrent response of Ru-Cu/CeO_2 (Fig. 2e) [39]. Obviously, Ru nanoparticles and Cu single atoms optimized the carrier transfer kinetics, facilitating fast electron supply and migration during the co-reduction of N_2 and CO_2 process over Ru-Cu/CeO_2. The only concern may be that the inadequate intrinsic photoelectron driving force in CeO_2 limits the delivery of the photocatalytic activity.

TPD tests were employed to explore the adsorption behaviours of N_2 and CO_2 molecules at different sites. As shown in the N_2-TPD spectra, no obvious desorption peaks were observed in CeO_2 and Cu/CeO_2 (Fig. S33 online). For Ru/CeO_2, the peak at 320 °C corresponded to the chemisorption of N_2 [40,41]. The intensity of the chemisorption peak in Ru-Cu/CeO_2 shows an obvious enhancement. When it comes to CO_2, the decoration of Ru nanoparticles barely enhanced CO_2 absorption intensity compared to CeO_2. Nevertheless, a desorption peak appeared at 330 °C over Cu/CeO_2, which is attributed to the chemisorption of CO_2. And the intensity was further improved in Ru-Cu/CeO_2. Apparently, Ru nanoparticles and Cu single atoms played specific roles in the adsorption of N_2 and CO_2, respectively, and their combination simultaneously benefited the optimal adsorption and conversion of N_2 and CO_2 in Ru-Cu/CeO_2. To further evidence this statement, we performed the independent reduction reaction with either CO_2 or N_2 as the feeding gas. Ru/CeO_2 exhibited the catalytic activity in N_2 reduction reaction (NRR) with an NH_3 yield rate of 29.6 μmol g^{-1} h^{-1}, but the activity in CO_2 reduction reaction (CO_2RR) was unsatisfactory (Fig. 2f). On the contrary, Cu/CeO_2 displayed inferior response in NRR, but promising catalytic performance toward CO_2-to-CO conversion (27.1 μmol g^{-1} h^{-1}). Evidently, Ru nanoparticles and Cu single atoms served as the active sites for N_2 and CO_2 transformation during urea synthesis, respectively.

After recognizing the roles of Ru and Cu sites, a question arises: how does the coupling between NRR and CO_2RR occur on Ru-Cu/CeO_2? We further monitored the structural evolution of Ru and Cu sites during urea synthesis by *in situ* XAFS characterizations. During *in situ* XAFS tests, the sample was immersed into N_2 and CO_2-saturated H_2O solution upon light illumination. As illustrated in Fig. 3a, relative to the initial Ru K-edge FT-EXAFS curve, an additional peak at around 1.4 Å emerged under reaction conditions. Given the relative highest adsorption tendency of N_2 at Ru site, the new peak was assigned to the Ru–N bond (Fig. S34 online). This point was further verified by that the simulated spectra of Ru site adsorbed with an N_2 molecule matched well with the experimental data (Fig. S35 online). The best fitting result implies the coordination number of Ru-N of 0.4. Notably, EXAFS analysis reflects the statistical average information, so the 0.4-fold Ru-N coordination suggests that a considerable amount of nitrogen-containing molecules accumulated over Ru nanoparticles. As for Cu species, the coordination peak intensity displays a slight increase at about 1.4 Å under reaction conditions over Ru-Cu/CeO_2 (Fig. 3b). In comparison, Cu/CeO_2 exhibited a higher increase under the same test condition. Owing to the stronger affinity with CO_2 at Cu sites, the increment was attributed to the Cu-C coordination formed between Cu single atoms and carbon-containing intermediates. And, the increased coordination numbers were determined as 0.2 and 0.9 in Ru-Cu/CeO_2 and Cu/CeO_2, respectively (Figs. S36–S39 online). The result suggests that more carbon-containing intermediates were consumed within the nitrogen-rich environment generated at Ru nanoparticles in Ru-Cu/CeO_2. In contrast, due to the lack of this consumption approach, most C species remained over Cu/CeO_2.

Moreover, *in situ* DRIFTS was performed to track the C-N coupling over the catalysts. The spectra were recorded after the saturated adsorption of feeding gas. As depicted in Fig. S40 (online), the signals of Ru-Cu/CeO_2 were almost unchanged without illumination over time, implying that the reaction was driven by light. As the light was introduced, Ru-Cu/CeO_2 exhibited gradually intensified *in situ* DRIFTS signals along with the prolonged illumination time. The characteristic signals of the stretching vibrations for C=O (1699 cm^{-1}) and C–O (1314 and 1025 cm^{-1}) emerged as CO_2 was introduced, which originated from the hydrogenation course of CO_2 to *COOH [5,18,42]. The band centered at 2921 cm^{-1} was

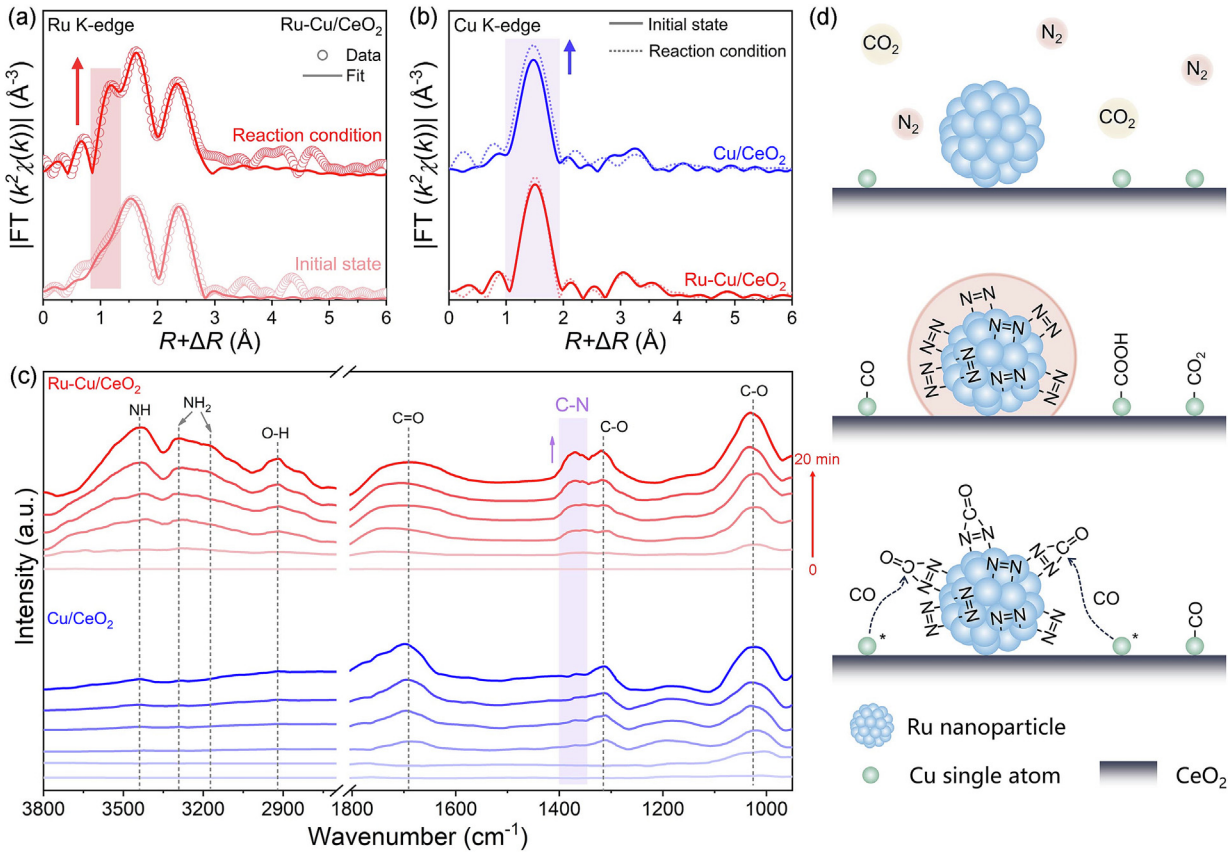

Fig. 3. Specific process tracking of C-N coupling over Ru-Cu/CeO_2. (a) *In situ* FT-EXAFS spectra at Ru K-edge of Ru-Cu/CeO_2 in *R* space. (b) *In situ* FT-EXAFS spectra at Cu K-edge of Cu/CeO_2 and Ru-Cu/CeO_2 in *R* space. (c) *In situ* DRIFTS spectra of Cu/CeO_2 and Ru-Cu/CeO_2 during photocatalytic urea synthesis. (d) Schematic diagram of *in situ* generated Ru-nitrogen moiety for enhancing C-N coupling over Ru-Cu/CeO_2.

observed as O–H stretching vibration [5,43]. When the feeding gas was N_2, the signal at 3441 cm^{-1} was attributed to the stretching vibration of NH, and the ones at 3291 and 3171 cm^{-1} corresponded to the stretching vibrations for NH_2 [5,44,45]. It is worth noting that except for these signals, the peak of the C–N stretching vibration was captured at 1370 cm^{-1} during urea synthesis over Ru-Cu/CeO_2, which is regarded as the decisive signal for C-N coupling [46,47]. Similar spectra were also recorded over Ru/CeO_2 and Cu/CeO_2. Despite the bit weaker C-N signal intensity of Ru/CeO_2 than Ru-Cu/CeO_2 due to the relatively insufficient supply of carbon-containing intermediates, Cu/CeO_2 even exhibits the weakest intensity. It demonstrates that the local nitrogen-rich Ru nanoparticle assisted realize the effective capture to carbon-containing intermediate for C-N coupling, which also explains the accelerated consumption of C species over Ru-Cu/CeO_2 than Cu/CeO_2.

In view of the experimental results, a possible reaction procedure over Ru-Cu/CeO_2 is depicted in Fig. 3d. N_2 molecules were first specifically adsorbed and activated on Ru nanoparticles, along with the protonation of CO_2 at Cu single atoms. The *in situ* generated local nitrogen-rich environment boosted the encounter probability with the carbon-containing intermediates generated at Cu sites, leading to the enhanced C-N coupling efficiency toward urea production.

DFT calculations were carried out to gain the in-depth insights in urea synthesis process (Figs. S41 and S42 online, Tables S7 and S8 online). The adsorption energies of N_2 and CO_2 at Ru and Cu sites are calculated, respectively. As shown in Fig. 4a, N2 molecule is strongly adsorbed at Ru sites with the adsorption energy of –0.86 eV, while the one at Cu site is –0.34 eV. In contrast, the adsorption intensity of CO_2 molecule at Cu sites is superior to that at Ru sites. As such, the specific adsorption at Ru and Cu sites leads to their different preference in N_2 or CO_2 activation during the urea synthesis reaction, which is consistent with the above experimental results. Moreover, we calculated the reaction barriers of CO_2-to-CO process over Cu sites (Fig. 4b). CO_2 molecule initially undergoes a protonation course to *COOH with the energy barrier of 0.18 eV, then transforms to *CO (ΔG = 0.13 eV). Notably, the subsequent desorption of *CO is an exothermic process. According to the previous reports, *NCON is typically regarded as the vital precursor toward urea synthesis (Fig. 4c) [5,6,18]. In this case, the spontaneous desorption of *CO ensures the supply of CO intermediate for the subsequent C-N coupling. The obvious increase in the urea yield rate when N_2 and CO as feeding gas also corroborated this point of view (Fig. S43 online). Meanwhile, the case that the protonation of *CO is highly endothermic excludes the possibilities of the conversion from CO_2 to other C-containing products (Fig. S44 online). We further screen the possible reaction pathway of urea formation over Ru-Cu/CeO_2 (Fig. 4d). N_2 molecule is first adsorbed on Ru nanoparticle. Then, the desorbed CO transfers to Ru site and couples with the adsorbed N_2 to generate *NCON. This step confronts a moderate kinetic barrier of ~1.04 eV (Fig. S45 online). Still, from the thermodynamical aspect, the Gibbs free energy variation of *NCON formation is determined as –0.17 eV, indicating the C-N coupling behaviour over Ru-Cu/CeO_2 is exothermic. Afterwards, *NCON undergoes several proton-electron coupling processes to form *NH_2CONH_2 rather than other by-products and ultimately release. Among them, except the last protonation process from *NH_2CONH to *NH_2CONH_2 involves overcoming an energy barrier of 0.27 eV, the others are all spontaneous.

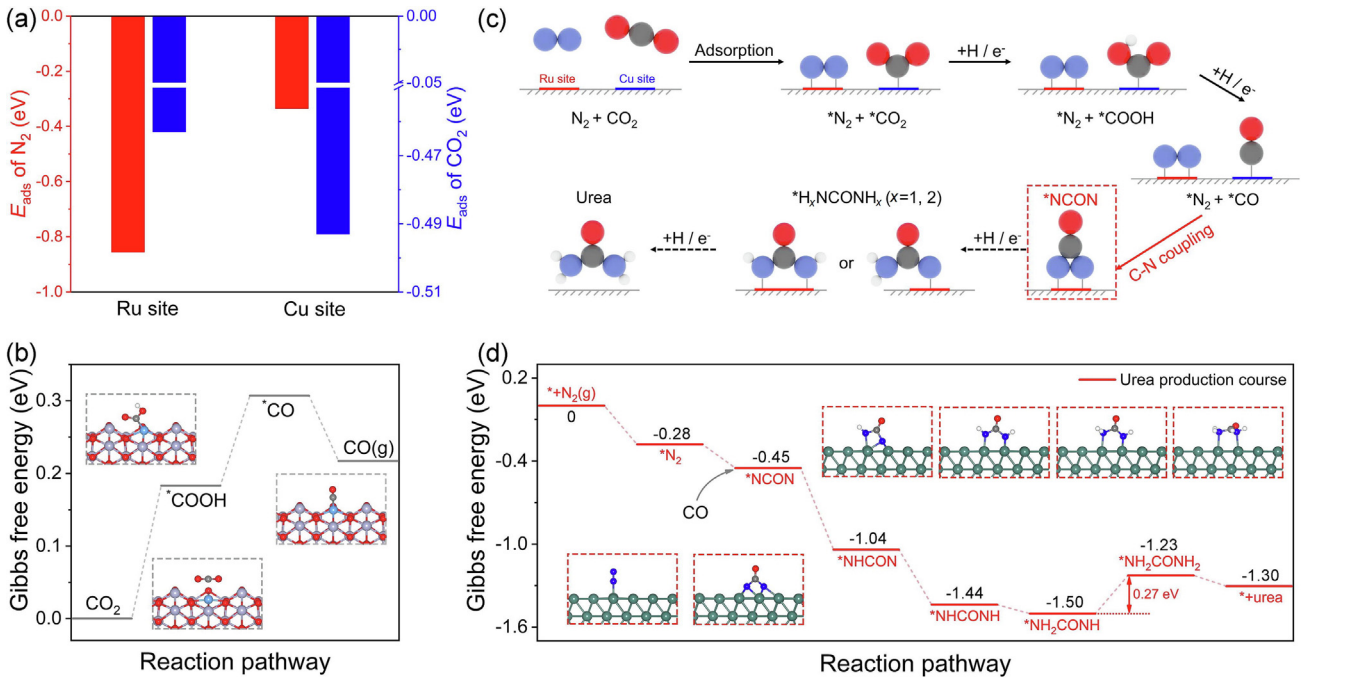

Fig. 4. Theoretical calculations of urea synthesis course. (a) Adsorption energy calculations of N_2 and CO_2 molecules at Ru and Cu sites, respectively. (b) Calculated Gibbs free energy diagram of photocatalytic CO_2RR to CO over Cu site. (c) Schematic diagram of the reaction pathway of urea synthesis. (d) Calculated Gibbs free energy diagram of urea production. The balls in white, grey, indigo, red, azure, green, and lavender represent H, C, N, O, Cu, Ru, and Ce atom, respectively.

4. Conclusion

In summary, an efficient multi-site photocatalyst consisting of CeO_2 with Ru nanoparticles and Cu single atoms is developed for urea synthesis. The simultaneous optimization in molecular activation and photogenerated carrier separation is crucial to the remarkable enhancement of urea photosynthesis performance over Ru-Cu/CeO_2. The experimental and theoretical results exhibit that Ru and Cu sites realized the accelerated electron kinetics as well as the site-selective N_2 and CO_2 conversion, significantly decreasing the energy barrier for the formation of the key *NCON intermediate. The boosted C-N coupling course positions Ru-Cu/CeO_2 among the best catalysts reported in photocatalytic urea synthesis. This work paves a new avenue for developing advanced catalysts with multiple functional sites towards various photocatalysis applications.

Conflict of interest

The authors declare that they have no conflict of interest.

Acknowledgments

This work was support by the National Natural Science Foundation of China (12222508, 12475325, and 22209061), the Youth Innovation Promotion Association CAS (2020454), the National Key R&D Program of China (2019YFA0405601 and 2023YFA1506304), the Fundamental Research Funds for the Universities of Inner Mongolia Autonomous Region (JY20250030), and the Start-up Fund for Senior Talents in Jiangsu University (21JDG060). The authors appreciate the Supercomputing system in the Supercomputing Center of USTC and the USTC center for Micro- and Nanoscale Research and Fabrication.

Author contributions

Xusheng Zheng and Wenping Sun conceived the idea. Qingyu Wang conducted the experiments and data analyses, and wrote the manuscript. Yangyang Wan, Qichen Liu, and Pengting Sun conducted the DFT calculations. Yida Zhang performed the XAFS data analyses. Zhentao Ma and Zirui Xu assisted to synthesize the samples. Hai-Long Jiang and Gongming Wang discussed the results. All authors contributed to the manuscript revision.

Appendix A. Supplementary material

Supplementary data to this article can be found online at https://doi.org/10.1016/j.scib.2025.01.059.

References

[1] Lv CD, Zhong LX, Liu HJ, et al. Selective electrocatalytic synthesis of urea with nitrate and carbon dioxide. Nat Sustain 2021;4:868–76.
[2] Sun HC, Li LF, Chen HC, et al. Highly efficient overall urea electrolysis via single-atomically active centers on layered double hydroxide. Sci Bull 2022;67:1763–75.
[3] Zhao YL, Ding YX, Li WL, et al. Efficient urea electrosynthesis from carbon dioxide and nitrate via alternating Cu-W bimetallic C-N coupling sites. Nat Commun 2023;14:4491.
[4] Fan XY, Liu CZ, He X, et al. Efficient electrochemical co-reduction of carbon dioxide and nitrate to urea with high faradaic efficiency on cobalt-based dual-sites. Adv Mater 2024;36:2401221.
[5] Chen C, Zhu XR, Wen XJ, et al. Coupling N_2 and CO_2 in H_2O to synthesize urea under ambient conditions. Nat Chem 2020;12:712–24.
[6] Luo YT, Xie B, Ou PF, et al. Selective electrochemical synthesis of urea from nitrate and CO_2 via relay catalysis on hybrid catalysts. Nat Catal 2023;6:939–48.
[7] Cao X, Zhang DW, Gao YQ, et al. Design of boron and transition metal embedded two-dimensional porous carbon nitride for electrocatalytic synthesis of urea. J Am Chem Soc 2024;146:1042–52.
[8] Mao CL, Byun J, MacLeod HW, et al. Green urea production for sustainable agriculture. Joule 2024;8:1224–38.

[9] Yang WP, Xiao L, Dai WD, et al. Efficient solar driven upgrading of N_2 to urea through photoredox reactions on Pt cluster/TiO_2. Adv Energy Mater 2024;14:2303806.
[10] Gao YH, Wang JN, Sun ML, et al. Tandem catalysts enabling efficient C-N ccoupling toward the electrosynthesis of urea. Angew Chem Int Ed 2024;63:e202402215.
[11] Wang Y, Xia S, Cai R, et al. Dynamic reconstruction of two-dimensional defective Bi nanosheets for efficient electrocatalytic urea synthesis. Angew Chem Int Ed 2024;63:e202318589.
[12] Liu JX, Smith SC, Gu YT, et al. C-N coupling enabled by N–N bond breaking for electrochemical urea production. Adv Funct Mater 2023;33:2305894.
[13] Song XW, Basheer C, Xia Y, et al. One-step formation of urea from carbon dioxide and nitrogen using water microdroplets. J Am Chem Soc 2023;145:25910–6.
[14] Hu Q, Zhou WL, Qi S, et al. Pulsed co-electrolysis of carbon dioxide and nitrate for sustainable urea synthesis. Nat Sustain 2024;7:442–51.
[15] Maimaiti H, Xu B, Sun J-Y, et al. Photocatalytic synthesis of urea (CO_2/N_2/H_2O) on coal-based carbon nanotubes with the Fe-core-supported Ti^{3+}-TiO_2 composite catalyst. ACS Sustain Chem Eng 2021;9:6991–7002.
[16] Chen XY, Lv SN, Gu HF, et al. Amorphous bismuth-tin oxide nanosheets with optimized C-N coupling for efficient urea synthesis. J Am Chem Soc 2024;146:13527–35.
[17] Li D, Zhao YX, Miao YX, et al. Accelerating electron-transfer dynamics by TiO_2-immobilized reversible single-atom copper for enhanced artificial photosynthesis of urea. Adv Mater 2022;34:2207793.
[18] Yang SY, Zhang WS, Pan GL, et al. Photocatalytic co-reduction of N_2 and CO_2 with CeO_2 catalyst for urea synthesis. Angew Chem Int Ed 2023;62:e202312076.
[19] Zhang YD, Sun YJ, Wang QY, et al. Synergy of photogenerated electrons and holes toward efficient photocatalytic urea synthesis from CO_2 and N_2. Angew Chem Int Ed 2024;63:e202405637.
[20] Shi CW, Xia K, Zhang LL, et al. Nitric acid-mediated artificial urea photosynthesis with N_2 and CO_2. Adv Energy Mater 2024;14:2400201.
[21] Chen J, Zhao DM, Diao ZD, et al. Ferrites boosting photocatalytic hydrogen evolution over graphitic carbon nitride: a case study of (Co, Ni)Fe_2O_4 modification. Sci Bull 2016;61:292–301.
[22] Kresse G, Hafner J. *Ab initio* molecular-dynamics simulation of the liquid-metal–amorphous-semiconductor transition in germanium. Phys Rev B 1994;49:14251–69.
[23] Kresse G, Furthmüller J. Efficient iterative schemes for *ab initio* total-energy calculations using a plane-wave basis set. Phys Rev B 1996;54:1169.
[24] Kresse G, Furthmüller J. Efficiency of *ab-initio* total energy calculations for metals and semiconductors using a plane-wave basis set. Comput Mater Sci 1996;6:15–50.
[25] Perdew JP, Chevary JA, Vosko SH, et al. Atoms, molecules, solids, and surfaces: applications of the generalized gradient approximation for exchange and correlation. Phys Rev B 1992;36:6671–87.
[26] Perdew JP, Burke K, Ernzerhof M. Generalized gradient approximation made simple. Phys Rev Lett 1996;77:3865–8.
[27] Grimme S, Antony J, Ehrlich S, et al. A consistent and accurate *ab initio* parametrization of density functional dispersion correction (DFT-D) for the 94 elements H-Pu. J Chem Phys 2010;132:154104.
[28] Nørskov JK, Rossmeisl J, Logadottir A, et al. Origin of the overpotential for oxygen reduction at a fuel-cell cathode. J Phys Chem B 2004;108:17886–92.
[29] Nørskov JK, Bligaard T, Logadottir A, et al. Trends in the exchange current for hydrogen evolution. J Electrochem Soc 2005;152:J23.
[30] Baroni S, Giannozzi P, Isaev E. Density-functional perturbation theory for quasi-harmonic calculations. Rev Mineral Geochem 2010;71:39–57.
[31] Ge J, He DS, Bai L, et al. Ordered porous Pd octahedra covered with monolayer Ru atoms. J Am Chem Soc 2015;137:14566–9.
[32] Li P, Zhou Y, Zhao ZY, et al. Hexahedron prism-anchored octahedronal CeO_2: crystal facet-based homojunction promoting efficient solar fuel synthesis. J Am Chem Soc 2015;137:9547–50.
[33] Saptal VB, Sasaki T, Bhanage BM. Ru@PsIL-catalyzed synthesis of N-formamides and benzimidazole by using carbon dioxide and dimethylamine borane. ChemCatChem 2018;10:2593.
[34] Li MY, Yang PP, Lv WJ, et al. Ultrastable ruthenium-based electrocatalysts for hydrogen oxidation reaction in high-temperature polymer electrolyte membrane fuel cells. CCS Chem 2024. https://doi.org/10.31635/ccschem.024.202404436.
[35] Wang QY, Zhang YD, Lin MX, et al. Photoinduced metastable asymmetric Cu single atoms for photoreduction of CO_2 to ethylene. Adv Energy Mater 2023;13:2302692.
[36] Xiao XD, Gao YT, Zhang LP, et al. A promoted charge separation/transfer system from Cu single atoms and C_3N_4 layers for efficient photocatalysis. Adv Mater 2020;32:2003082.
[37] Wang QY, Xiao Y, Yang SK, et al. Monitoring electron flow in nickel single-atom catalysts during nitrogen photofixation. Nano Lett 2022;22:10216–23.
[38] Wang L, Liu J, Wang HY, et al. Forming electron traps deactivates self-assembled crystalline organic nanosheets toward photocatalytic overall water splitting. Sci Bull 2021;66:265–74.
[39] Zhang YD, Ma ZT, Yang SK, et al. Element-dependent effects of alkali cations on nitrate reduction to ammonia. Sci Bull 2024;69:1100–8.
[40] Gao X, An L, Qu D, et al. Enhanced photocatalytic N_2 fixation by promoting N_2 adsorption with a co-catalyst. Sci Bull 2019;64:918–25.
[41] Wang PT, Ji YJ, Shao Q, et al. Core@shell structured Au@SnO_2 nanoparticles with improved N_2 adsorption/activation and electrical conductivity for efficient N_2 fixation. Sci Bull 2020;65:350–8.
[42] Dai DS, Fan MZ. Investigation of the dislocation of natural fibres by Fourier-transform infrared spectroscopy. Vib Spectrosc 2011;55:300–6.
[43] Ji SF, Jiang TL, Xu K, et al. FTIR study of the adsorption of water on ultradispersed diamond powder surface. Appl Surf Sci 1998;133:231–8.
[44] Coleman MM, Lee KH, Skrovanek DJ, et al. Hydrogen bonding in polymers. 4. Infrared temperature studies of a simple polyurethane. Macromolecules 1986;19:2149–57.
[45] Manivannan M, Rajendran S. Investigation of inhibitive action of urea-Zn^{2+} system in the corrosion control of carbon steel in sea water. Int J Eng Sci Technol 2011;3:8048–60.
[46] Zhang XR, Zhu XR, Bo SW, et al. Electrocatalytic urea synthesis with 63.5% faradaic efficiency and 100% N-selectivity via one-step C-N coupling. Angew Chem Int Ed 2023;62:e202305447.
[47] Yao DC, Miao W, Chu CC, et al. One-step pyrolysis conversion of glucose and urea into melanoidin for highly efficient photocatalytic H_2O_2 production. Chem Eng J 2023;467:143550.